

Depletion of COPI in cancer cells: the role of reactive oxygen species in the induction of lipid accumulation, noncanonical lipophagy and apoptosis

A. Gasparian^{a,†}, M. Aksenova^{a,†}, D. Oliver^{a,†}, E. Levina^b, R. Doran^a, M. Lucius^a, G. Pirolì^c, N. Oleinik^e, B. Ogretmen^e, K. Myhre^d, N. Frizzell^c, E. Broude^a, M. D. Wyatt^a, and M. Shtutman^{b,a,*}

^aDepartment of Drug Discovery and Biomedical Sciences, College of Pharmacy, ^bDepartment of Biological Sciences College of Art and Science, ^cDepartment of Pharmacology, Physiology & Neuroscience, School of Medicine, University of South Carolina, Columbia, SC 29208; ^dDepartment of Pathology, Division of Molecular and Cellular Pathology, University of Alabama at Birmingham, Birmingham, AL 35233; ^eDepartment of Biochemistry and Molecular Biology, Hollings Cancer Center, Medical University of South Carolina, Charleston, SC 29425

ABSTRACT The coatamer protein complex 1 (COPI) is a multisubunit complex that coats intracellular vesicles and is involved in intracellular protein trafficking. Recently we and others found that depletion of COPI complex subunits zeta (COPZ1) and delta (ARCN1) preferentially kills tumor cells relative to normal cells. Here we delineate the specific cellular effects and sequence of events of COPI complex depletion in tumor cells. We find that this depletion leads to the inhibition of mitochondrial oxidative phosphorylation and the elevation of reactive oxygen species (ROS) production, followed by accumulation of lipid droplets (LDs) and autophagy-associated proteins LC3-II and SQSTM1/p62 and, finally, apoptosis of the tumor cells. Inactivation of ROS in COPI-depleted cells with the mitochondrial-specific quencher, mitoquinone mesylate, attenuated apoptosis and markedly decreased both the size and the number of LDs. COPI depletion caused ROS-dependent accumulation of LC3-II and SQSTM1 which colocalizes with LDs. Lack of double-membrane autophagosomes and insensitivity to Atg5 deletion suggested an accumulation of a microlipophagy complex on the surface of LDs induced by depletion of the COPI complex. Our findings suggest a sequence of cellular events triggered by COPI depletion, starting with inhibition of oxidative phosphorylation, followed by ROS activation and accumulation of LDs and apoptosis.

Monitoring Editor

Robert Parton
University of Queensland

Received: Aug 26, 2021

Revised: Sep 28, 2022

Accepted: Oct 3, 2022

INTRODUCTION

The coatamer protein complex I (COPI)-coated vesicles are essential for retrograde trafficking between the Golgi apparatus and the endoplasmic reticulum, as well as intra-Golgi transport. The diverse diseases associated with defects or perturbations of this complex and these processes underscore the importance of the

COPI complex. The COPI complex consists of seven subunits: α , β , β' , γ , δ , ϵ , and ζ . In mammalian cells, pairs of highly homologous isoforms of γ and ζ subunits ($\gamma 1/\gamma 2$ and $\zeta 1/\zeta 2$) are expressed. All the subunits are required for the assembly of the complex and its function in vesicle formation. The small GTPase, Arf1, regulates

This article was published online ahead of print in MBoc in Press (<http://www.molbiolcell.org/cgi/doi/10.1091/mbc.E21-08-0420>) on October 12, 2022.

Disclosure statement: No potential conflict of interest was reported by the authors.

[†]Authors contributed equally.

*Address correspondence to: M. Shtutman (shtutmanm@cop.sc.edu).

Abbreviation used: ATGL, adipose triglyceride lipase; BODIPY, 4,4-difluoro-4-bora-3a,4a-diaza-s-indacene; BSA, bovine serum albumin; COPI, coatamer protein complex I; DCFDA, 2',7'-dichlorofluorescein diacetate; DGAT, acyl-CoA:diacylglycerol acyltransferase; EM, electron microscopy; FBS, fetal bovine

serum; JNK, c-Jun N-terminal kinase; LP, lipid droplet; MitoQ, mitoquinone mesylate; OCR, oxygen consumption rate; PBS, phosphate-buffered saline; PFA, paraformaldehyde; ROS, reactive oxygen species; TG, triglyceride; UPR, unfolded protein response.

© 2022 Gasparian *et al.* This article is distributed by The American Society for Cell Biology under license from the author(s). Two months after publication it is available to the public under an Attribution-NonCommercial-Share Alike 4.0 International Creative Commons License (<http://creativecommons.org/licenses/by-nc-sa/4.0>).

"ASCB®," "The American Society for Cell Biology®," and "Molecular Biology of the Cell®" are registered trademarks of The American Society for Cell Biology.

COPI recruitment and dissociation from the membrane. We became interested in this intriguing complex after discovering that the $\zeta 2$ subunit of COPI is commonly inactivated in cancer cells, which leaves them utterly dependent on COP $\zeta 1$ for COPI complex function and, therefore, selectively sensitive to inhibition of COP $\zeta 1$ (synthetic lethal) (Shtutman and Roninson, 2011; Oliver *et al.*, 2017).

In the course of these studies, we realized that the cellular regulation of the entire COPI complex and the coatomers is incompletely understood, in part because the complex is considered to perform housekeeping functions absolutely essential for cellular activity. However, there is accumulating evidence associating altered expression of COPI proteins with cancer development and progression. Work from our lab and others showed that down-regulation of the $\zeta 2$ subunit occurs in malignant melanoma, colon, bladder, prostate (Shtutman and Roninson, 2011), and thyroid cancer (Direnzo *et al.*, 2012; Anania *et al.*, 2017; Di Marco *et al.*, 2020). Moreover, COP22 is part of the network regulated by the MIST1 transcriptional factor (Direnzo *et al.*, 2012; Lo *et al.*, 2017) and the $\zeta 2$ subunit is involved in gastric cancer development (Hayakawa *et al.*, 2015). Elevated expression of the α and β subunits was associated with mesothelioma progression, prostate cancer, and ovarian cancer (Sudo *et al.*, 2010; Claerhout *et al.*, 2012; Maki-Nevala *et al.*, 2016; Mi *et al.*, 2016). Additionally, extensive mutations in the *COPG1* gene, encoding the γ subunit of COPI, have been found exclusively in asbestos-induced mesothelioma (Maki-Nevala *et al.*, 2016).

Because the COPI complex is essential for cellular activity, variations in the levels of individual COPI proteins in tumor cells and tumor mutational landscapes (Maki-Nevala *et al.*, 2016) cause tumor-specific vulnerabilities compared with normal cells by selectively targeting individual COPI components (Shtutman *et al.*, 2011). However, a better understanding of the cellular effects of depleting the COPI complex is first required. Many cellular events are reportedly associated with down-regulation of COPI-complex proteins, such as the production of reactive oxygen species (ROS), formation of lipid droplets (LDs), inhibition of autophagy, Golgi disruption, and activation of the unfolded protein response (UPR). However, a unified mechanism of the cellular events triggered by COPI complex deficiency is currently lacking.

Additionally, mutations in the genes of COPI complex proteins have recently been linked to hereditary diseases. The autoimmunity COPA syndrome manifests as inflammatory arthritis and interstitial lung disease caused by missense mutations in the *COPA* gene, which encodes the α subunit (Watkin *et al.*, 2015; Jensson *et al.*, 2017). A frameshift mutation of the δ subunit, encoded by the *ARCN1* gene, causes a disorder characterized by facial dysmorphism, severe micrognathia, rhizomelic shortening, and microcephalic dwarfism (Izumi *et al.*, 2016). In these hereditary syndromes, the activity and/or the level of the α or δ subunits are diminished. Therefore a better understanding of the cellular effects of depleting the COPI complex will help to determine the molecular pathological mechanisms of COPI-related syndromes and will aid new anticancer drug development.

This report comprehensively explores the consequences of COPI depletion by analyzing diverse endpoints in autophagy-proficient and autophagy-defective tumor cells. Our results document production of mitochondrial ROS as a major trigger of apoptosis in COPI-depleted cells. The increased ROS is generated as part of a positive feedback loop activated by impairment of mitochondrial activity and LD formation caused by COPI-complex depletion.

RESULTS

Mitochondrial activity and ROS production in COPI-depleted cells

To investigate the effects of COPI depletion, we chose prostate carcinoma (PC3 and DU145) and osteosarcoma (U2OS) cell lines. These cell lines demonstrated consistent knockdown efficiency in our previous studies (Shtutman *et al.*, 2011; Oliver *et al.*, 2017). The necessity of the COPI complex integrity for mitochondria homeostasis was demonstrated in yeast (Zabehzhinsky *et al.*, 2016; Zhang *et al.*, 2018), but to our knowledge this has not been studied in mammalian cells. The ~30% inhibition of mitochondrial ATP production and maximal respiration by siRNA knockdown of $\zeta 1$ -subunit (COPZ1) was detected 48 h posttransfection in PC3 cells. By 72 h, a more pronounced inhibition (~80% inhibition) of mitochondrial activity as measured by the loss of the oxygen consumption rate (OCR) was observed (Figure 1A; Supplemental Figure S1). c-Jun N-terminal kinase (JNK) activity is associated with the inhibition of mitochondrial activity, and inhibiting JNK relieves this inhibition (Lucero *et al.*, 2019). In agreement with this, inhibiting JNK activity with the selective JNK inhibitor SP600125 partially alleviated the inhibitory effects of COPZ1 knockdown (Supplemental Figure S1).

Impaired ATP production and reduced efficiency of oxidative phosphorylation can contribute to mitochondrial ROS production (Indo *et al.*, 2007). Indeed, the level of ROS detected by 2',7'-dichlorofluorescein diacetate (DCFDA) fluorescence is significantly increased in COPI-depleted PC3 cells. Colocalization of DCFDA and MitoNIR signals as measured by microscopy suggests that mitochondria are the major site of ROS accumulation induced by knockdown of the α -subunit (COPA) (Figure 1B). To further characterize ROS production, flow cytometry analysis was performed. Significantly elevated fluorescence of oxidized DCFDA was observed after knockdown of COPZ1 and COPA in PC3, DU145, and U2OS cells (Figure 1C and Supplemental Figure S2, A–C). As expected, treatment of COPI-depleted cells with the mitochondria-specific ROS quencher MitoQ (mitoquinone mesylate) decreased ROS levels in the cells with COPA or COPZ1 knockdown. In the cells transfected with the scrambled siRNA control, basal ROS levels were unaffected by MitoQ treatment (Figure 1C and Supplemental Figure S2, A–C). Because mitochondrial JNK is known to regulate cellular ROS (Chambers and LoGrasso, 2011), the effect of the JNK inhibitor SP600125 was also tested. JNK inhibition suppressed the elevation in ROS levels caused by COPI depletion in all three cell lines but largely did not affect basal ROS levels in the cells treated with control siRNA (Figure 1C and Supplemental Figure S2, A–C).

Inhibition of ROS production decreases the number and size of LDs in COPI-depleted cells

Depletion of the COPI complex has been shown to trigger the accumulation of LDs (Beller *et al.*, 2008), the storage organelles for neutral lipids (Olzmann and Carvalho, 2019). The effects of depleting COPA and COPZ1 by siRNA on LD formation were analyzed by fluorescent staining with 4,4-difluoro-4-bora-3a,4a-diaza-s-indacene (BODIPY) 493/503, a dye specific for neutral lipids (Figure 2A). Quantitation of LD number and LD size, presented as a size density distribution, shows that knockdown of either COPA or COPZ1 caused a drastic increase in droplet size in U2OS cells (Figure 2D) and in both the droplet size and the total number for PC3 and DU145 cells (Figure 2, B and C, and Supplemental Figure S2). Treatment of COPA- or COPZ1-depleted cells with MitoQ or the JNK inhibitor SP600125 significantly decreased the size and number of LDs (Figure 3; Supplemental Figure S4A), shifting the peaks of droplet size distributions back toward the size observed in control

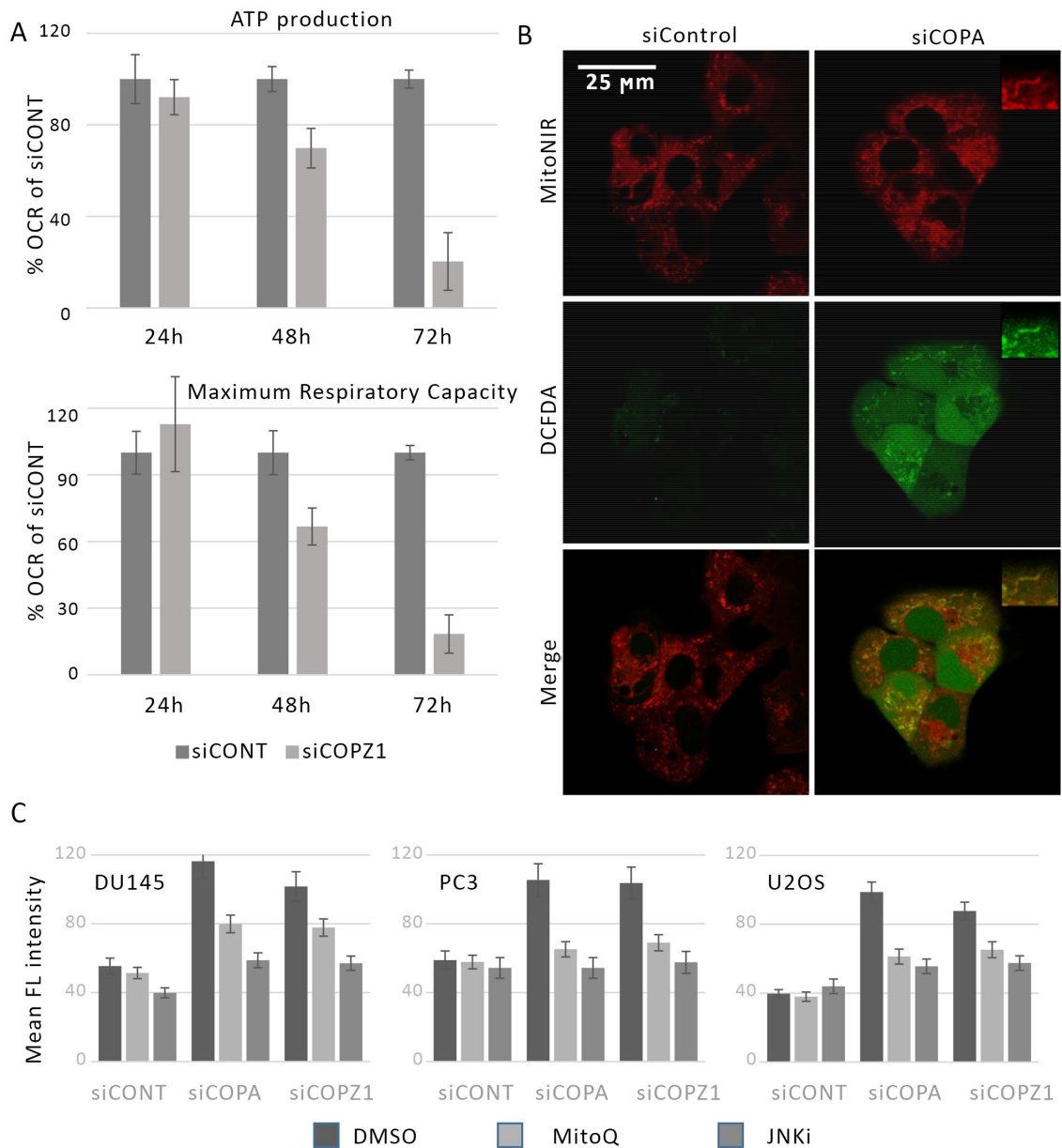


FIGURE 1: Depletion of the COPI complex inhibits mitochondrial activity and activates ROS production in tumor cell lines. (A) Measurements of mitochondrial metabolic activity. PC3 cells were transfected with control (siCONT) or anti COPZ1 (siCOPZ1) siRNAs and plated in Seahorse XF24 microplates. ATP production (upper panel), and maximum respiration capacity (lower panel) were detected by the OCR, see Supplemental Figure S1 for details. The bar graph shows the mean of four independent transfections \pm SE. (B) Measurement of induced mitochondrial ROS production in PC3 cells. PC3 cells were transfected with control (siCONT) or anti COPA (siCOPA) siRNAs. 72 h posttransfection ROS were detected with DCFDA, and mitochondria were stained with MitoNIR in live cells. Fluorescent images of separate and merged images are presented. (C) Summary of flow cytometry analysis of ROS production in COPI-depleted PC3, DU145, and U2OS cells and the effects of MitoQ and JNK inhibitor SP600125, labeled as JNKi (examples of flow cytometry profiles are presented in Supplemental Figure S2). Plots represent the DCFDA mean fluorescent intensity in siCONT, siCOPA, and siCOPZ1-transfected cells \pm MitoQ or SP600125 treatments. Results shown are three independent experiments per data point \pm SD. Scale bar = 25 μ m.

untreated cells (Supplemental Figure S4, C–E). Mean droplet area is also decreased by treatment with MitoQ and SP600125 (Figure 3B). The number of LDs per cell was also decreased with the most pronounced effects caused by inhibition of JNK activity (Figure 3C).

We further studied the dynamic effect of ROS quenching on the size of LDs. As above, siRNA depletion of COPA in PC3 cells resulted in the accumulation of large LDs 48 h posttransfection (Figure 4A). The size of the droplets did not change in vehicle-treated cells

(Figure 4A, upper panel, and Figure 4B, left panel; compare x-axis distribution in “siCOPA”). In contrast, the droplet size distribution drastically shifted toward smaller droplets after 8 h of treatment with MitoQ and size decreased further after 24 h (Figure 4A, lower panel, and Figure 4B, right panel; compare red 0-h peak to brown 8-h peak and cyan 24-h peak). Figure 4C shows that droplet size decreased in MitoQ-treated COPA-knockdown cells. In contrast, droplet size distribution was not affected in untreated COPA-depleted cells.

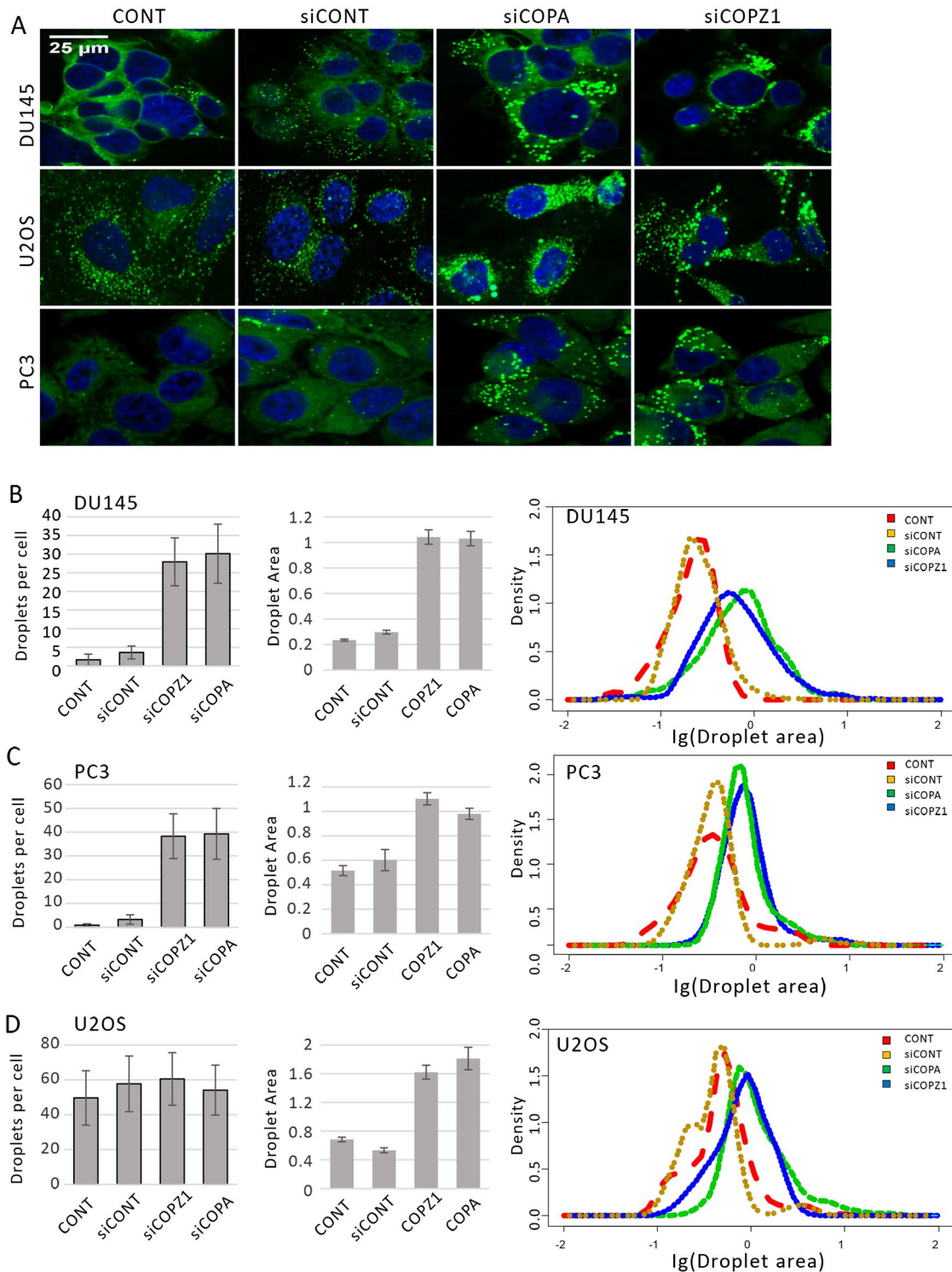


FIGURE 2: Depletion of the COPI complex induces the formation of LDs. PC3, U2OS, or DU145 cells were transfected with siCONT, siCOPA, and siCOPZ1; 72 h posttransfection, LDs and nuclei were visualized with BODIPY 493/503 (green) and DAPI (blue), respectively. (A). Fluorescent images of LDs in transfected cells. (B–D). Quantification of the effects of COPI complex depletion on the number and size of LDs in DU145 (B), PC3 (C), and U2OS (D) cells transfected with siRNAs. Plots in the left panels represent the mean of the number of the droplets per cell \pm SEM. The total number of LDs was quantified from fluorescent images of triplicate experiments (\sim 5 fields per experiment, 50–100 cells per data point). Plots in the middle panel represent the mean of droplet areas in transfected cells \pm SEM. The areas of the LDs (500–1300) per data point were obtained from three independent transfections. Plots in the right-hand panel show the distribution of droplet size in the transfected cells. Distributions are presented in a logarithmic scale. Scale bar = 25 μ m.

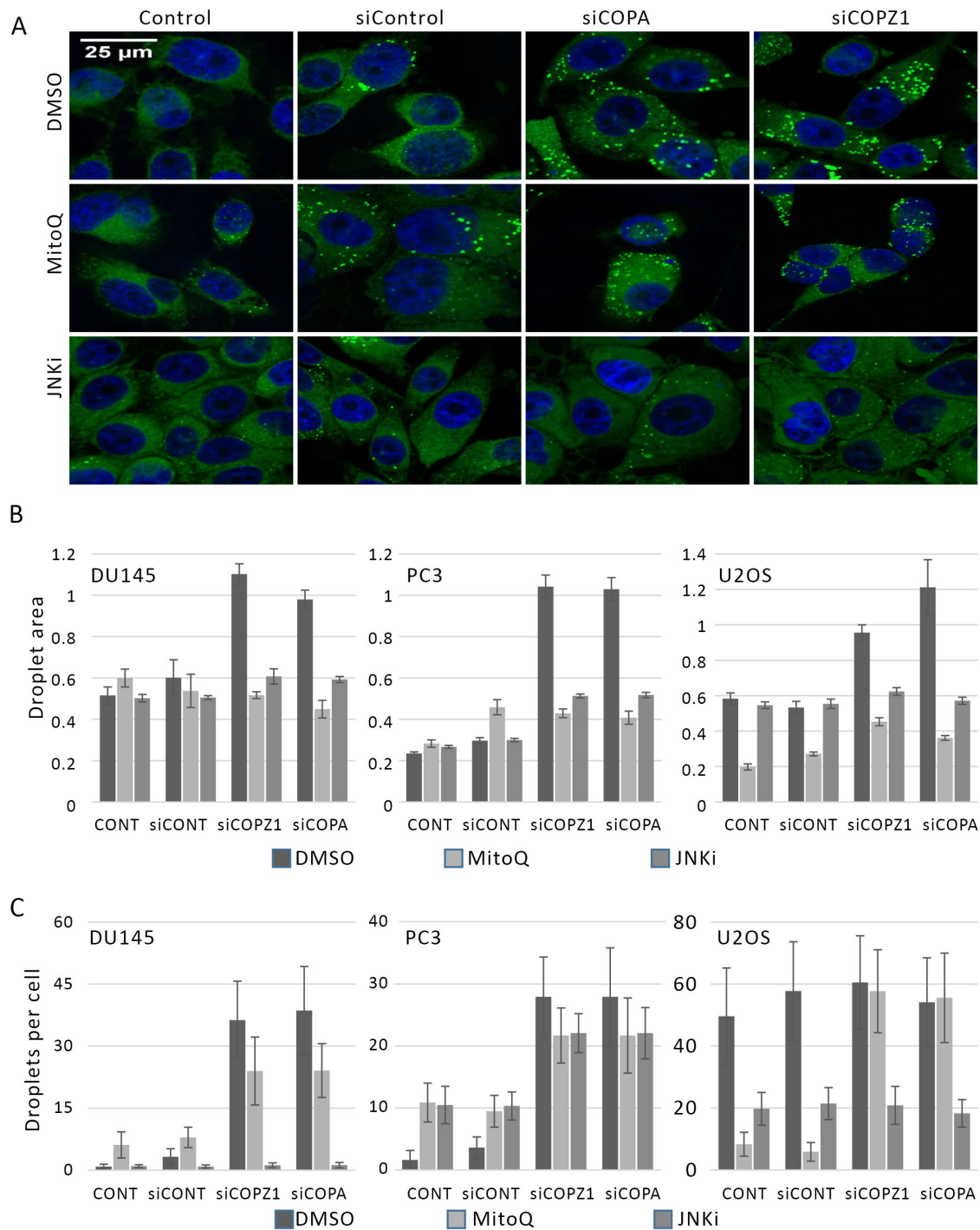


FIGURE 3: MitoQ and JNK inhibitor SP600125 decrease the size of LDs induced by depletion of COPI complex proteins. Cells were transfected with siCONT, siCOPA, and siCOPZ1 in triplicates. 48 h posttransfection cells were treated with MitoQ, JNK inhibitor, or vehicle control (DMSO) for an additional 24 h. (A) Representative fluorescent images of LDs (green) and nuclei (blue) visualized by BODIPY and DAPI staining, respectively, in the untransfected (control) and siRNA-transfected PC3 cells treated with JNK inhibitor, MitoQ, or vehicle (DMSO). Images of DU145 and U2OS cells are shown in Supplemental Figure S4, A and B. (B) Plots represent the mean of droplet areas in transfected cells \pm SEM. (C) Plots represent the mean of the number of the droplets per cells \pm SEM. Scale bar = 25 μ m.

Therefore ROS quenching in COPA-depleted PC3 cells decreased the size of LDs in a time-dependent manner.

The formation of droplets in COPI-depleted cells had previously been attributed to a decreased lipolysis rate due to loss of droplet-localized adipose triglyceride lipase (ATGL) (Beller *et al.*, 2008; Soni

et al., 2009). We therefore examined the impact of ROS caused by COPI depletion on lipolysis. Inhibition of ATGL activity in PC3 cells with a specific inhibitor, Atglistatin, increased the size of LDs, thus confirming the regulation of ATGL on LDs in these cells (Figure 5, A and B); as expected, Atglistatin inhibited lipolysis as determined by

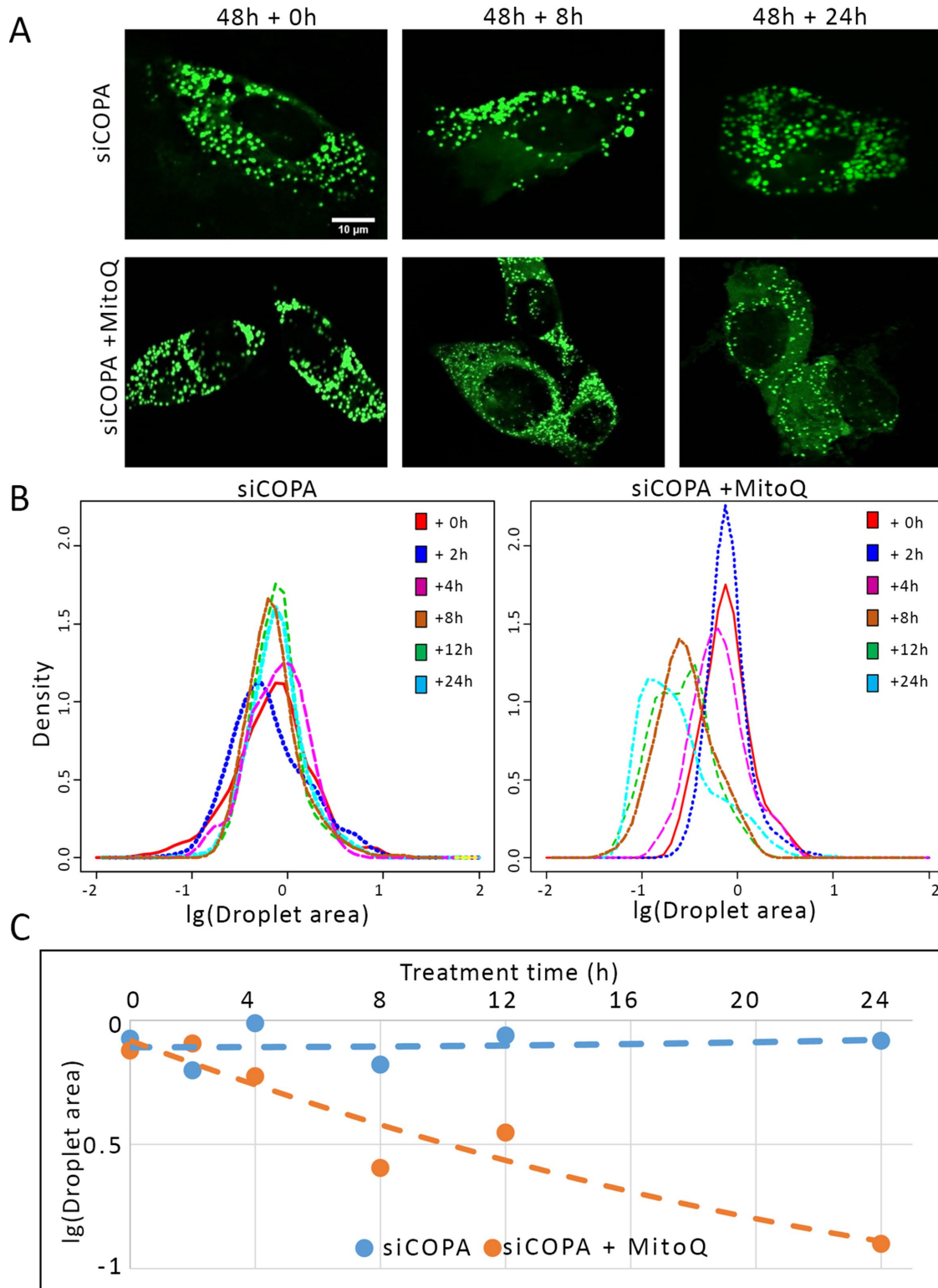


FIGURE 4: Time course of the decrease size of LDs in COPI-depleted cells by MitoQ treatment. PC3 cells were transfected with siCOPA; 48 h posttransfection, cells were treated with MitoQ or vehicle control up to 24 h. The cells were fixed at seven time points (0, 2, 4, 8, 12, and 24 h) followed by LD staining with BODIPY. (A) BODIPY staining of MitoQ-treated or vehicle-treated COPI-depleted cells. (B) Analysis of droplet size distribution. Plots show size distribution. The droplet area is shown in log₁₀ scale. (C) Plot represents maximums of droplet size distribution over time of MitoQ treatment. Scale bar = 10 μ m.

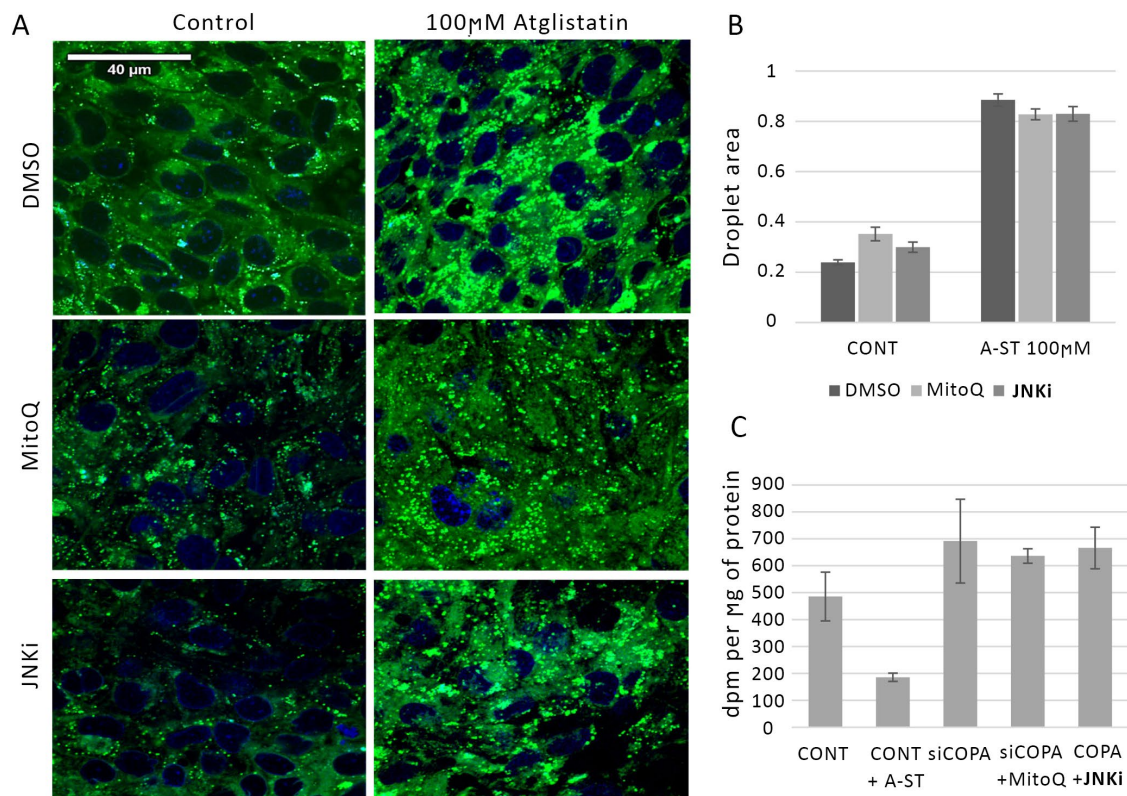


FIGURE 5: COPI depletion does not affect the rate of lipolysis and inhibition of lipolysis results in droplets insensitive to ROS depletion. (A) Representative immunofluorescence images of LDs in PC3 cells were treated with 100 μM Atglistatin for 48 h, ± MitoQ, JNK inhibitor, or DMSO (vehicle). LDs are visualized by BODIPY (green) and nuclei by DAPI (blue) staining. (B) Plot represents the average size of the LDs in the treated cells ± SEM. (C) Plot showing the release of [³H]-NEFA into the medium from cells treated with Atglistatin or transfected with siCOPA ± MitoQ or JNK inhibitor. The bars are the average of quadruplicates ± SEM. Scale bar = 40 μm.

radioactive lipolytic flux assay (Bezaire *et al.*, 2009) (Figure 5C). However, contrary to the LDs induced by COPI depletion, droplet size in Atglistatin-inhibited cells was unaffected by treatment with either MitoQ or SP600125 (Figure 5, A and B). The results suggest that the LDs induced by ATGL inhibition are not ROS dependent. Further, contrary to Atglistatin effects, depletion of COPA does not inhibit the lipolysis rate but rather slightly increases it. The increased lipolysis rate in COPA knockdown cells can be explained by the overall increase of the number of triglycerides (TGs). We next tested whether the treatment of COPA-depleted PC3 cells with MitoQ or SP600125 affects lipolysis and determined that these treatments do not affect the lipolysis rate (Figure 5C). Collectively, the results indicate that the accumulation of ROS results in the formation of LDs in COPI-depleted tumor cells in a manner that is not associated with inhibition of lipolysis rate catalyzed by ATGL. Furthermore, we determined the impact of inhibition of TG synthesis on LDs formation in COPI-depleted cells. TG synthesis is catalyzed by the evolutionarily unrelated acyl-CoA:diacylglycerol acyltransferase (DGAT) enzymes, DGAT1 and DGAT2, which catalyze the same reaction and account for nearly all TG synthesis (Chitraju *et al.*, 2019). Inhibition of both enzymes by selective inhibitors of DGAT1, PF-04620110 (Dow *et al.*, 2011), and DGAT2, PF-06424439 (Futatsugi *et al.*, 2015), decrease the number and size of LDs in both COPA-depleted cells and control cells (Supplemental Figure S8). However, COPI-depleted cells are less sensitive to DGAT1/2 inhibitors than control cells (Supplemental Figure S8). Therefore the results suggest that COPI depletion increases LD formation by a mechanism independent of DGATs.

Depletion of the COPI complex results in ROS-dependent accumulation of autophagy markers in LDs

Depletion of COPA or COPZ1 by siRNA substantially increased accumulation of the autophagy markers LC3II and SQSTM1/p62 in PC3 and U2OS cells as shown by WB analysis (Figure 6A). Knockdown of the COPI proteins in DU145 cells did not affect the levels of LC3 and p62 (Figure 6A). In DU145 cells, the *Atg5* gene lacks exon 6, which abolishes protein expression due to premature termination (Ouyang *et al.*, 2013) (Figure 6B). Because of the *Atg5* deficiency, DU145 cells express relatively high levels of p62 and LC3I (Figure 6A; see siCONT lane), which blocks the conversion to LC3II. Nonetheless, IF analysis of LC3-positive puncta, detected by staining with LC3-specific antibodies, shows the puncta accumulation in all three cell lines after depletion of the COPI proteins (Figure 6C, and Supplemental Figure S5, A and B). Analysis of LDs, visualized with BODIPY, shows that all LC3-positive puncta colocalized with LDs (Figure 6C and Supplemental Figure S5, A and B), while 30% (PC3) to 70% (DU145) of the LDs in COPI-depleted cells are positive for LC3 staining (Figure 6D). Therefore COPI depletion causes the induction of LC3-positive puncta that strongly colocalize with LDs regardless of *Atg5* status.

The inhibition of ROS production reduced the size and amount of LDs (Figures 3 and 4), and the level of LC3-positive puncta followed the same pattern. The IF results presented in Figure 7D and Supplemental Figure S6 confirms that the level of LC3-positive puncta drastically decreased in cells treated with MitoQ or the JNK inhibitor SP600125. The percentage of LC3-positive LDs correspondingly decreased (Figure 7C), suggesting that the extent of

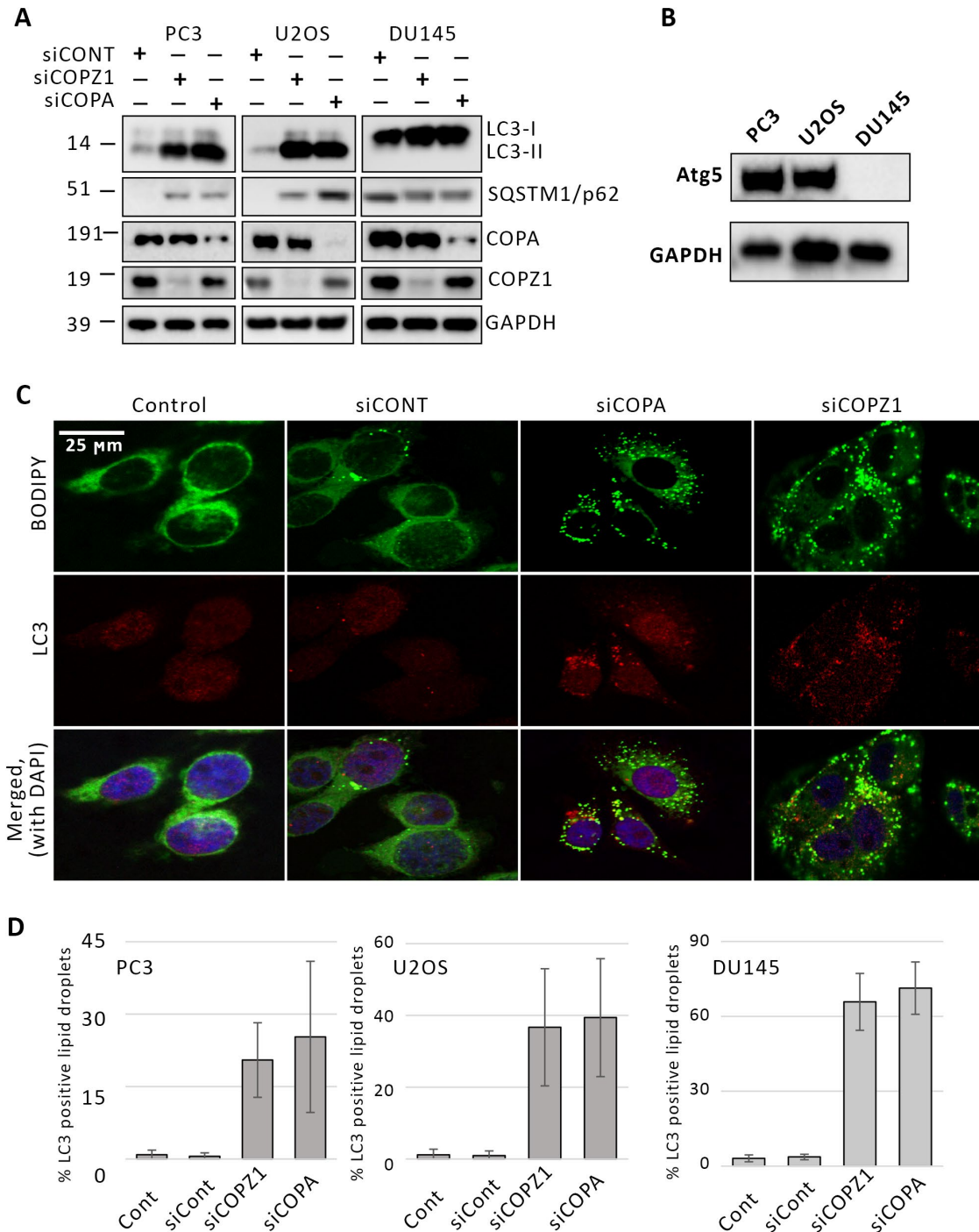


FIGURE 6: Depletion of the COPI elevates expression of markers of autophagy and number of LDs colocalized with autophagy markers. (A) Western blotting analysis of the expression of LC3 and p62/SQSTM1 in COPZ1 or COPA-depleted cells. (B) Western blotting analysis of Atg5 expression in PC3, U2OS, and DU145 cell lines. (C) Representative immunofluorescent images of LDs and LC3 in the control or siRNA-transfected PC3 cells; 72 h posttransfection, the LC3 was visualized by staining with specific antibodies (red), LDs by BODIPY (green), and nuclei by DAPI (blue) staining. Images of U2OS and DU145 cells are presented in Supplemental Figure S5. Scale bar = 25 μ m. (D) Quantification of LC3-positive LDs. The total number of LDs and the number of droplets positive for LC3 were determined. Plot represents the average quantification of at least 12 different fields from three independent transfections, \pm SEM.

LC3 and lipid colocalization depends on the size of the droplets. Treatment with MitoQ or the JNK inhibitor SP600125 decreased the level of autophagy markers LC3-II and SQSTM1 in wild type, Atg5-expressing U2OS and PC3 cells (Figure 7, A and B), further implicating ROS in the process of autophagy induced by COPI

depletion. Interestingly, the number of LC3-positive puncta also dramatically decreased in Atg5-deficient DU145 cells after treatment with MitoQ or SP600125 (Supplemental Figure S6B). This further suggests that both LC3-II and LC3-I may colocalize with the droplets.

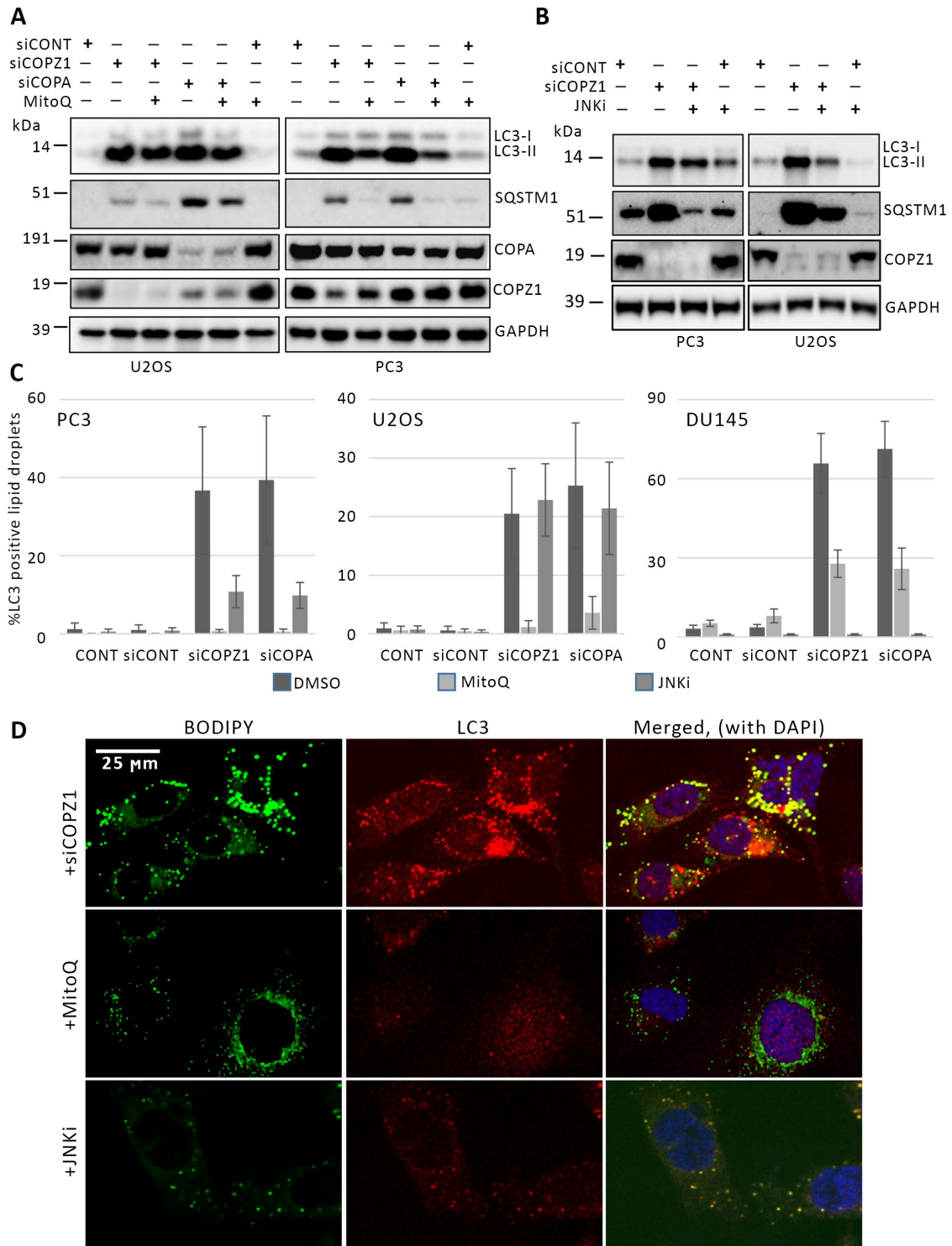


FIGURE 7: Treatment with MitoQ and JNK inhibitor decreases accumulation and colocalization of autophagic markers with LDs in COPI-depleted cells. U2OS and PC3 cells were transfected with siCONT, siCOPA, siCOPZ1, or mock transfection. MitoQ, SP600125, or vehicle control was added 48 h posttransfection; 72 h posttransfection, cells were either fixed or lysed for IF or Western blotting analysis. (A) Western blotting determination of the level of LC3-II and SQSTM1/p62 in COPA-depleted or COPZ1-depleted PC3 and U2OS cells treated with MitoQ. (B) Western blotting determination of the level of LC3-II and SQSTM1/p62 in COPZ1-depleted PC3 and U2OS cells treated with JNK inhibitor. (C) Quantification of LC3-positive LDs. The total number of LDs and the number of droplets positive for LC3 were determined. Plot represents the average of quantification of at least 12 different fields from three independent transfections, \pm SEM. (D) Representative immunofluorescent images of LDs (BODIPY, green) and LC3 (red) in the control or siCOPZ1-transfected PC3 cells, treated with MitoQ or JNK inhibitor. Images of U2OS and DU145 cells are presented in Supplemental Figure S6. Scale bar = 25 μ m.

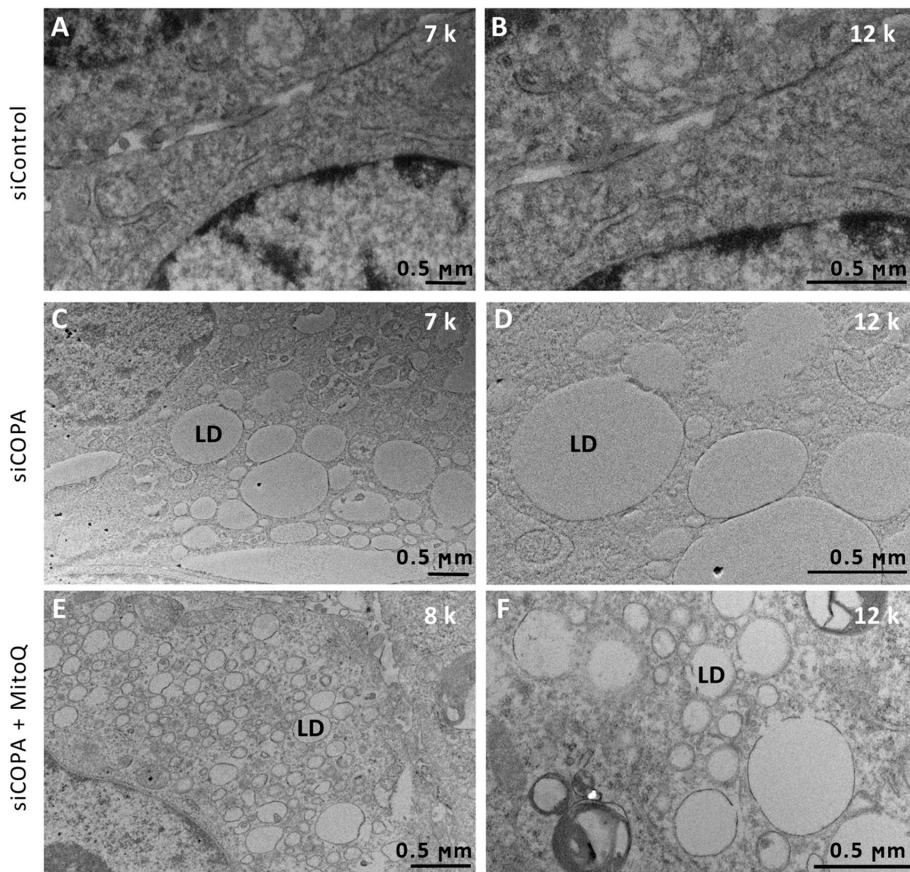


FIGURE 8: EM analysis of LDs in COPI knockdown cells did not reveal any accumulation of double-membrane autophagosomes. PC3 cells were transfected with siCONT or siCOPA for 48 h, then treated with MitoQ or vehicle control, followed by fixation at 72 h posttransfection. The structure of the droplets was analyzed by TEM with either low (7,000 \times or 8,000 \times) or high (12,000 \times) magnifications. Panels B and D show parts of panels A and C, respectively, at the higher magnifications. Panels E and F show separate areas taken at different magnifications. LDs = lipid droplets. Scale bar = 0.5 μ m.

The substantial accumulation of LC3-positive LD puncta after COPI depletion and the disappearance of LC3-positive puncta by ROS quenching suggest a potential activation of lipid-specific autophagy (lipophagy) in COPI-depleted cells. Activation of macrolipophagy predicts the formation of double-membrane autophagosome-like structures engulfing the droplets (Schott *et al.*, 2022), and that LD number may decrease upon the treatment of these cells with MitoQ or JNK inhibitor. Electron microscopy (EM) analysis of COPI-depleted cells confirmed the accumulation of massive LDs (Figure 8, A–D; Supplemental Figure S7, A and B). In agreement with the IF results (Figure 3 and Supplemental Figures S4, A and B), the size of the droplets significantly decreased with MitoQ treatment. However, the predicted accumulation of autophagosomes (up to 40% of all droplets based on LC3 and BODIPY colocalization results (Figure 6, C and D) was not observed in COPI-depleted cells. Autophagosome-like vesicles (multibody vesicles) were detected in these cells (Supplemental Figure S7E), but they were extremely rare relative to the LDs. Therefore the results suggest that although ROS induces accumulation of autophagy markers in COPI-depleted cells, the LDs that accumulate are not engulfed in mature autophagosomes in both autophagy-deficient (DU145) and autophagy-proficient PC3 and U2OS cells. Overall, the results show the characteristic features of noncanonical macrolipophagy, such as the assembly

of the autophagy complex on the surface of LDs (Schott *et al.*, 2022; Shroff and Nazarko, 2022) and independence from Atg5 activity (Schulze *et al.*, 2020).

COPI depletion induces apoptosis in an ROS-dependent manner and is fueled by exogenous lipids

TUNEL assay results in Figure 9A showed that knockdown of COPZ1 led to apoptosis and cell death in PC3, DU145, and U2OS cell lines. In agreement with the TUNEL assay results, knockdown of COPA and COPZ1 increased PARP cleavage as detected by WB (Figure 9B). The level of JNK phosphorylation measured with phospho-JNK-specific antibody also increased in COPI-depleted cells (Figure 9B). Treatment with the ROS quencher MitoQ decreased the level of PARP cleavage and JNK phosphorylation in both COPA and COPZ1 knockdown cells but not in the cells transfected with control siRNAs (Figure 9B). Treatment with SP600125 similarly attenuated apoptosis as detected by reduced accumulation of cleaved PARP back to control levels in COPZ1-depleted cells (Figure 9C).

The kinetics of cell death and apoptosis correlated with the number and size of droplets in COPI-depleted cells. Therefore we tested the effects of exogenous lipid treatment on lipid accumulation and the death of control and COPI-depleted cells. Treatment of the cells with oleic acid led to further accumulation of massive droplets in both control and siCOPA-transfected cells (not shown). Moreover, while the treatment of control siRNA-transfected cells did not significantly affect cell death, oleic acid treatment of COPA-knockdown cells drastically accelerated cell death 72 h posttransfection, when cell death level remains low in the absence of exogenous lipids at this time point (Figure 9A). Last, the percentage of dead cells correlated with oleic acid concentration (Figure 9D). The results show that COPI depletion induces apoptosis, which is attenuated by inhibiting ROS production and fueled by exogenous lipids.

DISCUSSION

This study provides a unified mechanism of the cellular events triggered by depletion of the COPI complex, including the first examination of the involvement of mitochondrial stress and ROS. Our results suggest the following model (Figure 10). Depletion of the COPI complex results in inhibition of mitochondrial oxidative phosphorylation, which in turn leads to the accumulation of ROS (Figure 1 and Supplemental Figures S1 and S2). The demonstration that COPI depletion disrupts mitochondrial function agrees with a recent study in a yeast model, namely, that COPI integrity and activity are essential for proper localization of mitochondrial proteins and mitochondrial activity (Zabezhinsky *et al.*, 2016). It is known that a decline in oxidative phosphorylation efficiency results in ROS overproduction (Indo *et al.*, 2007; Ishikawa *et al.*, 2008). Moreover, in agreement with our results, the activity of JNK was shown to be essential

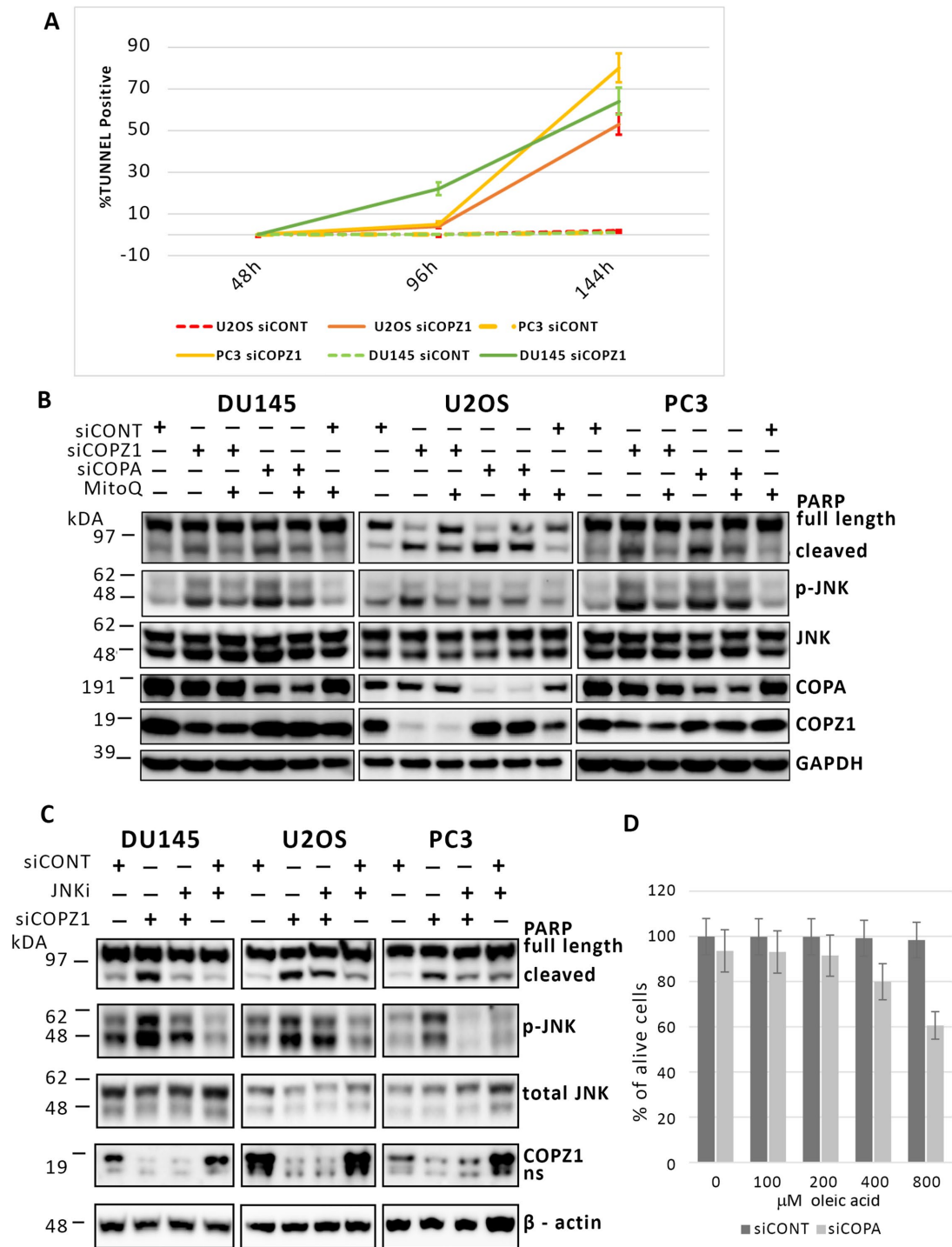


FIGURE 9: Apoptotic cell death in COPI-depleted cells is attenuated by MitoQ and a JNK inhibitor and increased by treatment with external lipids. (A) Depletion of the COPI complex induced apoptosis. U2OS, PC3, and DU145 cells were transfected either with control or COPZ1 siRNAs in triplicates. The percentage of apoptotic cells was determined by TUNEL assay. Plot shows the percentage of TUNEL positive cells \pm SD. (B) MitoQ effects on JNK phosphorylation and apoptosis. DU145, U2OS, or PC3 cells were transfected with siCONT, siCOPZ1 or siCOPA. 48 h posttransfection cells were treated with vehicle control or MitoQ. At 72 h cells were lysed and PARP cleavage, JNK phosphorylation, total level of JNK, COPA, and COPZ1 expression were determined by WB with the corresponding antibodies. (C). Effects of JNK inhibitor on JNK phosphorylation and apoptosis. DU145, U2OS, or PC3 cells were transfected with siCONT, or siCOPZ1. 48 h posttransfection cells were treated with vehicle control or JNK inhibitor. At 72 h cells were lysed and PARP cleavage, JNK phosphorylation, and total level of JNK, COPA, and COPZ1 expression were determined by Western blotting with the corresponding antibodies. (D). Depletion of the COPI complex sensitizes cells to lipotoxicity. U2OS cells were transfected with siCONT or siCOPA; 48 h posttransfection, cells were treated with different concentrations of oleic acids for 24 h. The percentage of dead cells was analyzed using live/dead viability/cytotoxicity assay. Plot represents dependence of percentage of alive ethidium homodimer-1 negative cells. Average of triplicates, \pm SE.

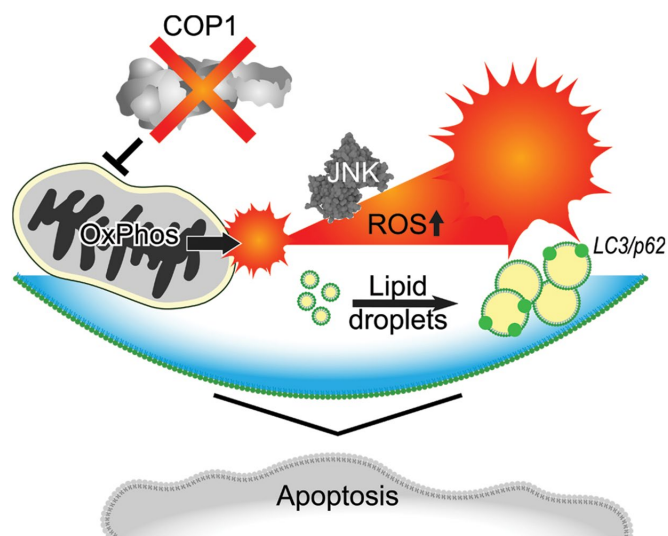


FIGURE 10: Scheme of the effects of COPI depletion in eukaryotic cells.

for mitochondrial ROS production, and JNK inhibition reduces mitochondrial ROS (Chambers and LoGrasso, 2011).

Experiments presented in Figure 2 (and Supplemental Figures S3 and S4) show that COPI depletion results in the increase of the number and size of the LDs. The inhibition of ROS levels by MitoQ and a JNK inhibitor prevents the LD accumulation (Figure 3). More strikingly, in COPI-depleted cells the quenching of ROS by MitoQ results in a drastic shrinkage of droplet size (Figure 4). Therefore the presented evidence establishes a causal link between ROS production and LD formation in COPI-depleted cells. However, the direct mechanism remains to be investigated. It was previously reported that knockdown of COPI complex proteins leads to the elevation of the number and size of LDs in cells (Nakamura *et al.*, 2005; Beller *et al.*, 2008; Guo *et al.*, 2008; Soni *et al.*, 2009; Thiam *et al.*, 2013; Wilfling *et al.*, 2014; Singh *et al.*, 2016; Li *et al.*, 2017). In COPI-depleted cells, LD formation can be directly caused by COPI loss as proposed above or can be caused by secondary events associated with ROS overproduction (Liu *et al.*, 2015; Welte and Gould, 2017).

Previously, the accumulation of LDs in COPI-depleted *Drosophila* S2 cells had been linked to the inhibition of the lipolysis rate (Beller *et al.*, 2008). Further, COPI complex integrity was shown to be important for ATGL delivery of LDs to the surface (Guo *et al.*, 2008; Soni *et al.*, 2009). However, our experiments presented in Figure 5 and Supplemental Figure S8 indicate that neither inhibition of lipolysis nor activation of TGs biosynthesis is the likely mechanism of LD accumulation in COPI-depleted cells. First, contrary to the effects of the ATGL inhibitor Atglistatin, COPI depletion does not decrease but rather slightly increases the lipolysis rate (Figure 5C). Second, despite a drastic effect on LD size and number, neither MitoQ nor JNKi affect the lipolysis rate in COPI-depleted cells. Inhibition of ATGL activity increases the size and number of LDs (Figure 5, A and B); however, in striking contrast with LDs induced by COPI depletion, Atglistatin-induced LDs are insensitive to MitoQ and JNKi (Figure 5B).

Additionally, we tested the effect of TG synthesis on LD formation in COPI-depleted cells. We determined the effects of inhibiting the DGAT enzymes DGAT1 and DGAT2, which catalyze the same reaction and account for nearly all TG synthesis (Chitraju *et al.*, 2019). Surprisingly, LD levels in COPI-depleted cells are less sensitive to DGAT inhibition in comparison with the control (Supplemen-

tal Figure S8). Thus since ROS may mediate phospholipid oxidation (Al-Saiedy *et al.*, 2018) and in turn affect the surfactant properties, our results are more consistent with a model suggesting that the decrease of droplet surface tension by the depletion of COPI complex leads to an increase in droplet size (Thiam *et al.*, 2013; Wilfling *et al.*, 2014).

COPI depletion leads to the accumulation of markers of autophagy on the surface of LDs in COPI-depleted cells (Figure 6). There are three important hallmarks indicated by our experiments: 1) lack of double-membrane canonical autophagosome (Figure 8), 2) Atg5-independent accumulation of LC3 on the surface of LDs, and 3) dependence of the level and the localization of the autophagy markers on the size of LDs, since these markers decreased along with LD size following MitoQ and JNK inhibitor treatments (Figure 7). The above results indicate the formation of a microlipophagy complex (Schulze *et al.*, 2020; Schott *et al.*, 2022; Shroff and Nazarko, 2022) on the LDs in COPI-depleted cells. Taken together, our results link ROS production, LD accumulation, and microlipophagy to COPI depletion (Figure 10). Apoptosis is also attenuated by inhibition of ROS and fueled by an excess of external fatty acids (Figure 9). Fatty acids are metabolized in tumor cells through beta oxidation (Donohoe *et al.*, 2012; Beloribi-Djefafalia *et al.*, 2016; Camarda *et al.*, 2016; Koizume and Miyagi, 2016). Thus the further fueling of damaged mitochondria with fatty acids increases ROS production (Barlow and Affourtit, 2013). Thus the results further highlight the central role of ROS in the multitude of events induced by COPI depletion (Figure 10). The inhibition of autophagy had been previously suggested to be a potential mechanism of the death of COPI-depleted cells (Claerhout *et al.*, 2012); however, the presented data are not supportive in the model.

The scope of the results presented here strongly supports the proposed mechanism (Figure 10). While the individual cellular events downstream of COPI depletion have previously been shown, the results shown here integrate the individual observations into the unified model (Figure 10).

Our model unifies multiple events triggered by depletion of the COPI complex and provides a framework for understanding the cellular impact of COPI malfunction or depletion in COPI-dependent genetic diseases, such as COPA syndrome, an immune dysregulatory disease characterized by polyarticular arthritis and progressive interstitial lung disease with pulmonary hemorrhages (Patwardhan and Spencer, 2019; Deng *et al.*, 2020; Lepelley *et al.*, 2020; Perrin *et al.*, 2020), COPA-associated Alzheimer's disease development (Astroski *et al.*, 2021), and COPB1-dependent neurodevelopmental abnormalities (Macken *et al.*, 2021).

The model also helps to elucidate the role of the COPI complex in tumor progression. Our previous and more recent results described the tumorigenic and premetastatic activities of the COPB2 subunit (Mi *et al.*, 2018; Pu *et al.*, 2018; An *et al.*, 2019; Bhandari *et al.*, 2019; Feng *et al.*, 2021; Zhang *et al.*, 2021) and tumor dependencies of the integrity of the COPI complex, specifically COPB, COPZ1, and ARCN1 (Shtutman *et al.*, 2011; Oliver *et al.*, 2017; Di Marco *et al.*, 2020; Wang *et al.*, 2020). The results could serve as a framework for further development of COPI—complex targeting cancer therapy.

MATERIALS AND METHODS

[Request a protocol](#) through *Bio-protocol*.

Cell lines and reagents

U2OS human osteosarcoma cells, HeLa human cervical carcinoma, DU145, and PC3 human prostate carcinoma cells were obtained

from American Type Culture Collection (Manassas, VA). Cells were cultured in high glucose DMEM, supplemented with penicillin, streptomycin, and glutamine (HyClone reagents from GE Healthcare Life Sciences, Pittsburgh, PA), and 10% fetal bovine serum (FBS; MediaTech Inc., Manassas, VA). Life Technologies OptiMEM 1 reduced serum medium for siRNA transfection experiments was from Life Technologies/Fisher Scientific (Hampton, NH). SiLentFect lipid reagent for siRNA transfection was from Bio-Rad (Hercules, CA). During passaging cells were checked for the absence of mycoplasma contamination using the MycoFluor Mycoplasma detection kit (Thermo Fisher Scientific, Waltham, MA). Cell line authentication was performed at the University of Arizona Genetics Core (Tucson, AZ).

Unless otherwise noted, all chemicals were purchased from Sigma-Aldrich Chemical Co (St. Louis, MO and Milwaukee, WI). Selective JNK inhibitor SP600125 was from Tocris (Minneapolis, MN). Adipose tryglyceride lipase inhibitor Atglistatin, DGAT2 inhibitor PF-06424439, and DGAT1 inhibitor PF-04620110 were from Cayman Chemical Co (Ann Arbor, MI). Mitochondria-targeted ROS antioxidant MitoQ (MitoQ10) was from MedKoo Biosciences (Morrisville, NC). CytoPainter MitoNIR indicator reagent was from Abcam (Cambridge, MA). General oxidative stress indicator carboxy-H2DCFDA was from Thermo Fisher Scientific (Waltham, MA). Invitrogen TRIzol RNA isolation reagent was from Thermo Scientific (Rockford, IL).

Knockdown of COPZ1 and COPA genes

The knockdown experiment had been performed in 6 well plates, with 100,000–300,000 cells per well. Cells were reversely transfected with 10 nM ON-TARGET Plus SMART pool human COPZ1 siRNA or human COPA siRNA (Thermo Scientific Dharmacon, Lafayette, CO) using siLentFect lipid reagent (Bio-Rad, Hercules, CA) as recommended by the manufacturer. Transfection with All Stars Negative Control siRNA (Qiagen, Germantown, MD) was used as a negative control for the potential siRNA off-target effects. Knockdown efficiency was evaluated using Western blot analysis with a corresponding antibody.

Measurement of OCR

PC3 prostate carcinoma cells were reversely transfected with the indicated siRNA as described above and 6 h after transfection cells were collected and seeded in a regular cell culture medium (DMEM+10% FBS+antibiotics) on Seahorse XF24 cell culture microplate (Agilent Technologies, Santa Clara, CA) coated with 0.2% gelatin at a density of 50,000 cells per well. The Seahorse extracellular flux analyzer 24 (XF-24, Agilent Technologies) was used to measure the OCR 24, 48, 72, and 96 h after transfection. XF assay medium was supplemented with 1 mM sodium pyruvate and 25 mM glucose. After measurement of basal respiration, oligomycin (5 µg/ml), carbonyl cyanide 4-(trifluoromethoxy) phenylhydrazone (1.25 µM), and rotenone/antimycin A (3 µM/4 µM) were added sequentially to determine ATP production/proton leak, spare respiratory capacity, and nonmitochondrial respiration. After completion of the assay, the cells were washed with phosphate-buffered saline (PBS) and stored at –70°C prior to the measurement of the total protein content using the BCA protein assay (Thermo Fisher Scientific).

Analysis of mitochondrial localization of ROS using fluorescent microscopy

Cells were transfected with siCOPA or siControl. 24 h later, transfected cells were replated onto 35/10 mm glass bottom 4 compartment plates (Greiner Bio-One, GmbH, Frickenhausen, Germany, Cat

No. 627870), and 48 h later cell incubation with DCFDA was performed as described below. Instead of DCFDA, transfected cells were also incubated with a vehicle (DMSO) and were used later for staining with CytoPainter MitoNIR indicator reagent (Abcam) alone. After DCFDA-containing medium was removed, cells were washed and incubated with CytoPainter MitoNIR indicator reagent (Abcam) as recommended by the manufacturer. DCFDA-treated cells were also incubated with HBSS buffer without MitoNIR indicator reagent. Cells were washed, filled with DMEM without phenol red, and observed using a fluorescent microscope with specific filter sets: for DCFDA, Ex./Em. 482 nm/536 nm; for CytoPainter, 640 nm/659 nm.

Quantitative ROS detection using flow cytometry

Cells were reversely transfected with the indicated siRNAs. ROS detection was performed 72 h after transfection. MitoQ or SP600125 were added 24 h before ROS detection. Cells were washed, loaded with 10 µM DCFDA in serum-free culture medium, and incubated for 45 min in CO₂ incubator, followed by quick (2–3 min) trypsinization and cell resuspension in ice-cold serum-free medium. Cells were kept on wet ice, in the dark, until analysis by flow cytometry. For a positive control cells were incubated with freshly prepared 0.1 mM hydrogen peroxide for 20 min followed by triple wash and incubation with DCFDA as described above. For a negative control, cells were incubated in media without DCFDA. Cells transfected with negative control siRNA and incubated with DCFDA were also used as a negative control. DCFDA fluorescence was detected by flow cytometry using the FITC channel on an LSRII flow cytometer (BD Biosciences, San Jose, CA).

BODIPY 493/503 staining of neutral LDs and analysis of colocalization with autophagic proteins

Cells were reversely transfected with siCOPZ1, siCOPA, and negative control siRNA as described above in 6-well plates, 200,000 cells per well. Cells treated with siLentFect lipid reagent along were used as an additional negative control. 24 h after transfection cells were replated into 12-well plates with inserted round glass coverslips. 24 h later cells were treated with 300 nM MitoQ, 25 µM SP600125, or vehicle (DMSO) for additional 24 h. Then cells were rinsed with PBS and fixed with 4% paraformaldehyde (PFA) for 10 min. Fixed cells were rinsed again and permeabilized with 0.1% Triton X-100 in PBS for 10 min at room temperature. Cells were stained with 2 mM BODIPY 493/503 (Molecular Probes/Fisher Scientific [Hampton, NH]) mixed with DAPI for 1 h at room temperature in the dark followed by wash with 0.01% Tween 20 in PBS. After addition of PBS, cells were visualized with 40x objective (LD Plan NeoFluor 0.6 MA) using Zeiss 700 confocal microscope (Carl Zeiss Meditec, Dublin, CA). Immediately after preliminary visualization, rabbit anti-LC3B antibodies (Cell Signaling Technology, Cat No.3868, dilution 1:200) were added to the cells and incubated for 2 h at room temperature on a rocker platform followed by 1 h incubation with Alexa Fluor 594 donkey anti-rabbit secondary antibody (Thermo Scientific, 1:500 dilution). Cells were rinsed with PBS, and glass coverslips were mounted on glass slides using VECTASHIELD HardSet mounting medium (Vector Laboratories, Burlingame, CA). Next-day images were taken with 63x objective (Plan APO 1.4) using Zeiss 700 confocal microscope.

ImageJ software (National Institutes of Health, USA) was used to analyze the amount and size of the LDs after the images were acquired using a Zeiss 700 confocal microscope. Green channel was changed to gray using lookup table and then the image was inverted to improve contrast. “Particle analyzer” option was used with size set from 4 to infinity, capturing the number and size of the

droplets simultaneously in one spreadsheet. DAPI images were then used to manually count the number of cells and calculate the amount of LDs per cell.

For colocalization analysis of green LDs with red LC3-positive puncta we used ImageJ "Image calculator" option. Red channel and green channel were first analyzed separately, getting the numbers of red and green particles for each channel. Then both inverted green and red channels were merged, creating a new window, and then the number of resulting particles were analyzed.

Sodium oleate treatment

U2OS cells were transfected with siControl or siCOPA as described above. 48 h posttransfection cells were treated with different concentrations (200 μ M, 400 μ M and 800 μ M) of oleic acid for 24 h. Sodium oleate stock was prepared in dd H₂O supplemented with 4% fatty acid-free BSA (bovine serum albumin). The percentage of dead cells was analyzed by flow cytometry using Live/Dead Viability/Cytotoxicity assay kit (Invitrogen/Thermo Fisher Scientific).

Atglistatin treatment

PC3 prostate carcinoma cells were plated in a 12-well plate with coverslip glass inserts as described above and treated with 50 or 100 μ M of Atglistatin for 48 h either with or without MitoQ and SP600125. MitoQ, SP600125, or vehicle (DMSO) was added 24 h after the addition of Atglistatin. The cells were fixed with 4% PFA following by LD staining with BODIPY as described above. Images were obtained using a fluorescent microscope, and droplet size distribution was analyzed as described earlier using about 300–1000 droplets per data point.

Treatment with the inhibitors of DGATs, DGAT1, and DGAT2

PC3 prostate carcinoma cells were transfected with siCOPA or All-Stars negative control siRNA mix as above. Six hours after transfection, these cells were treated with the following: a selective DGAT2 inhibitor PF-06424439 (10 μ M), a selective DGAT1 inhibitor PF-04620110 (10 μ M), their combination, or vehicle (DMSO); 72 h after transfection, these cells were stained with BODIPY 493/503. Cell nuclei were counterstained with NucBlue Live Cell Stain ReadyProbes reagent (Thermo Fisher Scientific Invitrogen). Droplet size and number were analyzed as above.

Lipolytic flux measurement by the release of nonesterified fatty acids to the medium from cells pretreated with [³H]-oleic acid

Whole-cell lipolysis was determined as described (Bezaire *et al.*, 2009). PC3 cells were transfected with siCOPA, and after 48 h posttransfection cells were treated with MitoQ, SP600125, or vehicle control for 24 h. Alternatively, nontransfected control cells were treated with 100 μ M of Atglistatin for 24 h. At the same time [³H]-oleic acid ([³H]-OA) was added to all the samples in quadruplicate wells (fixed concentration 0.5 μ Ci/well, specific activity 54.5 Ci/mmol; PerkinElmer Life and Analytical Sciences, Boston, MA) for 24-h incubation. The [³H]-OA is incorporated into TGs (Homan *et al.*, 1991). Following incubation, cells were washed with fresh medium containing 4% fatty acid-free BSA to remove nonincorporated [³H]-OA. Medium was replaced with fresh MEM containing an extremely low amount of FBS (0.1%), and then 10 μ M Triascin C (Cayman Chemicals Co, Ann Arbor, MI) was added to each well. The Triascin C, an inhibitor of acetyl-CoA synthase, was added to circumvent complications in cultured cells caused by re-esterification flux of fatty acids. Cells were returned to the incubator and 50 μ l of medium samples were collected at 0 h to establish a baseline, 1, 2,

and 4 h. Finally, cells were washed with PBS and solubilized in RIPA buffer, and protein concentration was determined using Bio Rad DC (detergent compatible) protein assay. Radioactivity was measured in the medium samples using a liquid scintillation counter (model Tri-Carb 2900TR; PerkinElmer Life and Analytical Sciences, Waltham, MA). The results were normalized by protein concentration as a measurement of the number of plated cells.

TEM analysis of LDs in COPI-depleted cells

For EM, PC3 cells were reversely transfected with siCOPA as described above in 6-well plates, 200,000 cells per well; 24 h after transfection, cells were replated into 12-well plates, and 24 h later cells were treated with 300 nM MitoQ or vehicle (DMSO) for additional 24 h. Cells were collected and centrifuged at a very low speed (1400 rpm) and fixed overnight in cacodylate-buffered 2.5% glutaraldehyde at 4°C. Cells were then postfixed in cacodylate-buffered 2% osmium tetroxide followed by ethanol and acetone dehydration and embedding in EMBed 812 resin (EMS). Ultrathin sections were stained with uranyl acetate and viewed on a Hitachi H-8000 transmission electron microscope at 7000–8000 \times and at 15,000 \times .

Preparation of cell lysates and Western blot analysis

Cells were washed and lysed in TNT buffer (20 mM Tris, pH 8.0, 200 mM NaCl, 1% Triton X-100) containing 1 mM DTT, EDTA-free Pierce protease inhibitor tablet, and Pierce phosphatase inhibitor tablet (Thermo Scientific, Rockford, IL) and then centrifuged for 10 min at 10,000 \times g, 4°C. Twenty micrograms of total protein per sample were analyzed by Western blotting using precast 4–12% or 4–15% gradient gels and buffers from Genscript (Piscataway, NJ). After protein transfer, membranes were stained with Ponceau red, blocked for 1 h in TBST buffer containing 5% nonfat dry milk, and incubated with a primary antibody overnight at 4°C. Primary antibodies used were from Cell Signaling Technology (Danvers, MA): PARP (Cat. No. 9532), phospho-SAPK/JNK (T183/Y185, Cat. No. 4668), SAPK/JNK (Cat. No. 9252), LC-3B (Cat. No. 3868), Atg5 (Cat. No. 12994), and β -Actin (Cat. No. 4970); from Santa Cruz Biotechnology (Dallas, TX): p62/SQSTM1 (Cat. No. sc-28359) and GAPDH (Cat. No. sc-32233). COPZ1 and COPA immune serum was a generous gift of Felix T. Wieland (Heidelberg University, Germany). After incubation with secondary antibody (Thermo Scientific, Cat. Nos. 31460 or 31430, depending on the host of the primary antibody), membranes were processed with chemoluminescent reagents: Pierce ECL Western Blotting Substrate or SuperSignal West Femto Maximum Sensitivity Substrate (Thermo Scientific). The maximum sensitivity reagent was used for the analysis of phospho-JNK, and PARP. The digital images were obtained using the ChemiDoc Touch Imaging System (Bio-Rad, Hercules, CA).

Apoptosis detection

Cells were trypsinized and collected by centrifugation at 300 \times g for 5 min and resuspended in 0.5 ml of 1% BSA in PBS. Resuspended cells were fixed by dropwise addition of 0.5 ml of freshly prepared 1% PFA in PBS for 15 min. PFA was removed and cells were washed with 1% BSA in PBS before the addition of 100% ethanol (2 ml dropwise). Fixed cells were stored at –20°C. Following fixation, cells were permeabilized and labeled using Cell Death Detection Kit (Roche, Basel, Switzerland). The number of TUNEL-positive cells was determined by flow cytometry using BD LSR II Flow Cytometer (BD Biosciences, NJ). PARP cleavage was detected using Western blotting.

Statistical analysis

The LD area results were log-transformed to conform to normality. The pairwise density distribution comparison was performed with a nonparametric permutation test of equity by `sm.density.compare` function (<https://cran.r-project.org/web/packages/sm/sm.pdf>) with the 1000 samples generated in bootstraps (`nboot = 1000`) (Bowman and Azzalini, 1997). The bootstrap bands are represented in cyan (see Supplemental Figure S3 as an example).

ACKNOWLEDGMENTS

We thank Igor Roninson and Taras Nazarko (Georgia State University, Atlanta, GA) for critical reading of our manuscript; we thank B. Celia Cui and Alexandra Sikirzhyski for help with the preparation of publication-quality figures. We thank Microscopy and Flow cytometry core and core director Vitali Sikirzhyski, UofSC COBRE Center for Targeted Therapeutics for the help with image acquisition and analysis and flow cytometry analysis.

REFERENCES

- Al-Saiedy M, Pratt R, Lai P, Kerek E, Joyce H, Prenner E, Green F, Ling CC, Veldhuizen R, Ghadorah S, et al. (2018). Dysfunction of pulmonary surfactant mediated by phospholipid oxidation is cholesterol-dependent. *Biochim Biophys Acta* 1862, 1040–1049.
- An C, Li H, Zhang X, Wang J, Qiang Y, Ye X, Li Q, Guan Q, Zhou Y (2019). Silencing of COPB2 inhibits the proliferation of gastric cancer cells and induces apoptosis via suppression of the RTK signaling pathway. *Int J Oncol* 54, 1195–1208.
- Anania MC, Cetti E, Lecis D, Todoerti K, Gulino A, Mauro G, Di Marco T, Cleris L, Pagliardini S, Manenti G, et al. (2017). Targeting COPZ1 non-oncogene addiction counteracts the viability of thyroid tumor cells. *Cancer Lett* 410, 201–211.
- Astroski JW, Akpoye LK, Androphy EJ, Custer SK (2021). Mutations in the COPI coatomer subunit α -COP induce release of A β -42 and amyloid precursor protein intracellular domain and increase tau oligomerization and release. *Neurobiol Aging* 101, 57–69.
- Barlow J, Affourtit C (2013). Novel insights into pancreatic beta-cell glucolipotoxicity from real-time functional analysis of mitochondrial energy metabolism in INS-1E insulinoma cells. *Biochem J* 456, 417–426.
- Beller M, Sztalryd C, Southall N, Bell M, Jäckle H, Auld DS, Oliver B (2008). COPI complex is a regulator of lipid homeostasis. *PLoS Biol* 6, e292.
- Beloribi-Djefaflija S, Vasseur S, Guillaumond F (2016). Lipid metabolic reprogramming in cancer cells. *Oncogenesis* 5, e189.
- Bezaire V, Mairal A, Ribet C, Lefort C, Grousse A, Jocken J, Laurencikiene J, Anesia R, Rodriguez AM, Ryden M, et al. (2009). Contribution of adipose triglyceride lipase and hormone-sensitive lipase to lipolysis in hMADS adipocytes. *J Biol Chem* 284, 18282–18291.
- Bhandari A, Zheng C, Sindan N, Sindan N, Quan R, Xia E, Thapa Y, Tamang D, Wang O, Ye X, et al. (2019). COPB2 is up-regulated in breast cancer and plays a vital role in the metastasis via N-cadherin and Vimentin. *J Cell Mol Med* 23, 5235–5245.
- Bowman AW, Azzalini A (1997). *Applied smoothing techniques for data analysis: the kernel approach with S-Plus illustrations*. Oxford, UK: OUP Oxford.
- Camarda R, Zhou AY, Kohnz RA, Balakrishnan S, Mahieu C, Anderton B, Eyob H, Kajimura S, Tward A, Krings G, et al. (2016). Inhibition of fatty acid oxidation as a therapy for MYC-overexpressing triple-negative breast cancer. *Nat Med* 22, 427–432.
- Chambers JW, LoGrasso PV (2011). Mitochondrial c-Jun N-terminal kinase (JNK) signaling initiates physiological changes resulting in amplification of reactive oxygen species generation. *J Biol Chem* 286, 16052–16062.
- Chitruju C, Walther TC, Farese RV Jr (2019). The triglyceride synthesis enzymes DGAT1 and DGAT2 have distinct and overlapping functions in adipocytes. *J Lipid Res* 60, 1112–1120.
- Claerhout S, Dutta B, Bossuyt W, Zhang F, Nguyen-Charles C, Dennison JB, Yu Q, Yu S, Balazsi G, Lu Y, et al. (2012). Abortive autophagy induces endoplasmic reticulum stress and cell death in cancer cells. *PLoS one* 7, e39400.
- Deng Z, Law CS, Ho FO, Wang KM, Jones KD, Shin JS, Shum AK (2020). A defect in thymic tolerance causes T cell-mediated autoimmunity in a murine model of COPA syndrome. *J Immunol* 204, 2360–2373.
- Di Marco T, Bianchi F, Sfondrini L, Todoerti K, Bongarzone I, Maffioli EM, Tedeschi G, Mazzoni M, Pagliardini S, Pellegrini S, et al. (2020). COPZ1 depletion in thyroid tumor cells triggers type I IFN response and immunogenic cell death. *Cancer Lett* 476, 106–119.
- Direnzo D, Hess DA, Damsz B, Hallett JE, Marshall B, Goswami C, Liu Y, Deering T, Macdonald RJ, Konieczny SF (2012). Induced Mist1 expression promotes remodeling of mouse pancreatic acinar cells. *Gastroenterology* 143, 469–480.
- Donohoe DR, Collins LB, Wali A, Bigler R, Sun W, Bultman SJ (2012). The Warburg effect dictates the mechanism of butyrate-mediated histone acetylation and cell proliferation. *Mol Cell* 48, 612–626.
- Dow RL, Li JC, Pence MP, Gibbs EM, LaPerle JL, Litchfield J, Piotrowski DW, Munchhof MJ, Manion TB, Zavadoski WJ, et al. (2011). Discovery of PF-04620110, a potent, selective, and orally bioavailable inhibitor of DGAT-1. *ACS Med Chem Lett* 2, 407–412.
- Feng Y, Lei X, Zhang L, Wan H, Pan H, Wu J, Zou M, Zhu L, Mi Y (2021). COPB2: a transport protein with multifaceted roles in cancer development and progression. *Clin Transl Oncol* 23, 2195–2205.
- Futatsugi K, Kung DW, Orr ST, Cabral S, Hepworth D, Aspnes G, Bader S, Bian J, Boehm M, Carpino PA, et al. (2015). Discovery and optimization of imidazopyridine-based inhibitors of diacylglycerol acyltransferase 2 (DGAT2). *J Med Chem* 58, 7173–7185.
- Guo Y, Walther TC, Rao M, Stuurman N, Goshima G, Terayama K, Wong JS, Vale RD, Walter P, Farese RV (2008). Functional genomic screen reveals genes involved in lipid-droplet formation and utilization. *Nature* 453, 657–661.
- Hayakawa Y, Ariyama H, Stancikova J, Sakitani K, Asfaha S, Renz BW, Dubeykovskaya ZA, Shibata W, Wang H, Westphalen CB, et al. (2015). Mist1 expressing gastric stem cells maintain the normal and neoplastic gastric epithelium and are supported by a perivascular stem cell niche. *Cancer Cell* 28, 800–814.
- Homan R, Grossman JE, Pownall HJ (1991). Differential effects of eicosapentaenoic acid and oleic acid on lipid synthesis and secretion by HepG2 cells. *J Lipid Res* 32, 231–241.
- Indo HP, Davidson M, Yen HC, Suenaga S, Tomita K, Nishii T, Higuchi M, Koga Y, Ozawa T, Majima HJ (2007). Evidence of ROS generation by mitochondria in cells with impaired electron transport chain and mitochondrial DNA damage. *Mitochondrion* 7, 106–118.
- Ishikawa K, Takenaga K, Akimoto M, Koshikawa N, Yamaguchi A, Imanishi H, Nakada K, Honma Y, Hayashi J (2008). ROS-generating mitochondrial DNA mutations can regulate tumor cell metastasis. *Science* 320, 661–664.
- Izumi K, Brett M, Nishi E, Drunat S, Tan ES, Fujiki K, Lebon S, Cham B, Masuda K, Arakawa M, et al. (2016). ARCN1 mutations cause a recognizable craniofacial syndrome due to COPI-mediated transport defects. *Am J Hum Genet* 99, 451–459.
- Jensson BO, Hansdottir S, Arnadottir GA, Sulem G, Kristjansson RP, Oddsson A, Benonisdottir S, Jonsson H, Helgason A, Saemundsdottir J, et al. (2017). COPA syndrome in an Icelandic family caused by a recurrent missense mutation in COPA. *BMC medical genetics* 18, 129.
- Koizume S, Miyagi Y (2016). Lipid droplets: a key cellular organelle associated with cancer cell survival under normoxia and hypoxia. *Int J of Mol Sci* 17, 1430.
- Lepelletier A, Martin-Niëlós MJ, Le Bihan M, Marsh JA, Uggenti C, Rice GI, Bondet V, Duffy D, Hertzog J, Rehwinkel J, et al. (2020). Mutations in COPA lead to abnormal trafficking of STING to the Golgi and interferon signaling. *J Exp Med* 217, e20200600.
- Li C, Luo X, Zhao S, Siu GK, Liang Y, Chan HC, Satoh A, Yu SS (2017). COPI-TRAPP II activates Rab18 and regulates its lipid droplet association. *EMBO J* 36, 441–457.
- Liu L, Zhang K, Sandoval H, Yamamoto S, Jaiswal M, Sanz E, Li Z, Hui J, Graham BH, Quintana A, et al. (2015). Glial lipid droplets and ROS induced by mitochondrial defects promote neurodegeneration. *Cell* 160, 177–190.
- Lo HG, Jin RU, Sibbel G, Liu D, Karki A, Joens MS, Madison BB, Zhang B, Blanc V, Fitzpatrick JA, et al. (2017). A single transcription factor is sufficient to induce and maintain secretory cell architecture. *Genes Dev* 31, 154–171.
- Lucero M, Suarez AE, Chambers JW (2019). Phosphoregulation on mitochondria: Integration of cell and organelle responses. *CNS Neurosci Ther* 25, 837–858.
- Macken WL, Godwin A, Wheway G, Stals K, Nazlamova L, Ellard S, Alfarez A, Aloraini T, AlSubaie L, AlFadhel M, et al. (2021). Biallelic variants in COPB1 cause a novel, severe intellectual disability syndrome with cataracts and variable microcephaly. *Genome Med* 13, 34.
- Maki-Nevala S, Sarhadi VK, Knuutila A, Scheinin I, Ellonen P, Lagstrom S, Ronty M, Kettunen E, Husgafvel-Pursiainen K, Wolff H, et al. (2016). Driver gene and novel mutations in asbestos-exposed lung

- adenocarcinoma and malignant mesothelioma detected by exome sequencing. *Lung* 194, 125–135.
- Mi Y, Sun C, Wei B, Sun F, Guo Y, Hu Q, Ding W, Zhu L, Xia G (2018). Coatamer subunit beta 2 (COPB2), identified by label-free quantitative proteomics, regulates cell proliferation and apoptosis in human prostate carcinoma cells. *Biochem Biophys Res Commun* 495, 473–480.
- Mi Y, Yu M, Zhang L, Sun C, Wei B, Ding W, Zhu Y, Tang J, Xia G, Zhu L (2016). COPB2 is upregulated in prostate cancer and regulates PC-3 cell proliferation, cell cycle, and apoptosis. *Arch Med Res* 47, 411–418.
- Nakamura N, Banno Y, Tamiya-Koizumi K (2005). Arf1-dependent PLD1 is localized to oleic acid-induced lipid droplets in NIH3T3 cells. *Biochem Biophys Res Commun* 335, 117–123.
- Oliver D, Ji H, Liu P, Gasparian A, Gardiner E, Lee S, Zenteno A, Perinskaya LO, Chen M, Buckhaults P, et al. (2017). Identification of novel cancer therapeutic targets using a designed and pooled shRNA library screen. *Sci Rep* 7, 43023.
- Olzmann JA, Carvalho P (2019). Dynamics and functions of lipid droplets. *Nat Rev Mol Cell Biol* 20, 137–155.
- Ouyang DY, Xu LH, He XH, Zhang YT, Zeng LH, Cai JY, Ren S (2013). Autophagy is differentially induced in prostate cancer LNCaP, DU145 and PC-3 cells via distinct splicing profiles of ATG5. *Autophagy* 9, 20–32.
- Patwardhan A, Spencer CH (2019). An unprecedented COPA gene mutation in two patients in the same family: comparative clinical analysis of newly reported patients with other known COPA gene mutations. *Pediatr Rheumatol Online J* 17, 59.
- Perrin J, Roux N, Maurier F (2020). Coatamer-associated protein subunit alpha syndrome: abnormal trafficking between the Golgi complex and the endoplasmic reticulum. *BMJ Case Rep* 13, e231553.
- Pu X, Wang J, Li W, Fan W, Wang L, Mao Y, Yang S, Liu S, Xu J, Lv Z, et al. (2018). COPB2 promotes cell proliferation and tumorigenesis through up-regulating YAP1 expression in lung adenocarcinoma cells. *Biomed Pharmacother* 103, 373–380.
- Schott MB, Rozeveld CN, Weller SG, McNiven MA (2022). Lipophagy at a glance. *J Cell Sci* 135, jcs259402.
- Schulze RJ, Krueger EW, Weller SG, Johnson KM, Casey CA, Schott MB, McNiven MA (2020). Direct lysosome-based autophagy of lipid droplets in hepatocytes. *Proc Natl Acad Sci USA* 117, 32443–32452.
- Shroff A, Nazarko TY (2022). SQSTM1, lipid droplets and current state of their lipophagy affairs. *Autophagy*, 1–4.
- Shtutman M, Baig M, Levina E, Hurteau G, Lim CU, Broude E, Nikiforov M, Harkins TT, Carmack CS, Ding Y, et al. (2011). Tumor-specific silencing of COP22 gene encoding coatamer protein complex subunit zeta 2 renders tumor cells dependent on its paralogous gene COP21. *Proc Natl Acad Sci USA* 108, 12449–12454.
- Shtutman M, Roninson IB (2011). A subunit of coatamer protein complex offers a novel tumor-specific target through a surprising mechanism. *Autophagy* 7, 1551–1552.
- Singh SR, Zeng X, Zhao J, Liu Y, Hou G, Liu H, Hou SX (2016). The lipolysis pathway sustains normal and transformed stem cells in adult *Drosophila*. *Nature* 538, 109–113.
- Soni KG, Mardones GA, Sougrat R, Smirnova E, Jackson CL, Bonifacino JS (2009). Coatamer-dependent protein delivery to lipid droplets. *J Cell Sci* 122, 1834–1841.
- Sudo H, Tsuji AB, Sugyo A, Kohda M, Sogawa C, Yoshida C, Harada YN, Hino O, Saga T (2010). Knockdown of COPA, identified by loss-of-function screen, induces apoptosis and suppresses tumor growth in mesothelioma mouse model. *Genomics* 95, 210–216.
- Thiam AR, Antonny B, Wang J, Delacotte J, Wilfling F, Walther TC, Beck R, Rothman JE, Pincet F (2013). COPI buds 60-nm lipid droplets from reconstituted water-phospholipid-triacylglyceride interfaces, suggesting a tension clamp function. *Proc Natl Acad Sci USA* 110, 13244–13249.
- Wang Y, Xie G, Li M, Du J, Wang M (2020). COPB2 gene silencing inhibits colorectal cancer cell proliferation and induces apoptosis via the JNK/c-Jun signaling pathway. *PLoS one* 15, e0240106.
- Watkin LB, Jessen B, Wiszniewski W, Vece TJ, Jan M, Sha Y, Thamsen M, Santos-Cortez RL, Lee K, Gambin T, et al. (2015). COPA mutations impair ER-Golgi transport and cause hereditary autoimmune-mediated lung disease and arthritis. *Nat Genet* 47, 654–660.
- Welte MA, Gould AP (2017). Lipid droplet functions beyond energy storage. *Biochim Biophys Acta* 1862, 1260–1272.
- Wilfling F, Thiam AR, Olarte MJ, Wang J, Beck R, Gould TJ, Allgeyer ES, Pincet F, Bewersdorf J, Farese RV Jr, et al. (2014). Arf1/COPI machinery acts directly on lipid droplets and enables their connection to the ER for protein targeting. *Elife* 3, e01607.
- Zabehzinsky D, Slobodin B, Rapaport D, Gerst JE (2016). An Essential Role for COPI in mRNA Localization to Mitochondria and Mitochondrial Function. *Cell Rep* 15, 540–549.
- Zhang B, Yu Q, Huo D, Li J, Liang C, Li H, Yi X, Xiao C, Zhang D, Li M (2018). Arf1 regulates the ER-mitochondria encounter structure (ERMES) in a reactive oxygen species-dependent manner. *Febs J* 285, 2004–2018.
- Zhang J, Wang X, Li G, He J, Lu Z, Yang Y, Jiang Y, Jiang L, Li F, Liu J (2021). COPB2: a novel prognostic biomarker that affects progression of HCC. *Biomed Res Int* 2021, 6648078.